Extended Source Interferometry in the Compact Regime

Bruno Pelle, Gregory W. Hoth, Stefan Riedl, John Kitching, and Elizabeth A. Donley
Time and Frequency Division
National Institute of Standards and Technology
Boulder, CO, USA
bruno.pelle@nist.gov

***Abstract*—We present an atom interferometer based on an expanding cloud of laser-cooled atoms sensitive to rotations along two axes and acceleration along one axis in an effective volume of 1 cm^3. We observed spatially resolved fringes created by the apparatus' rotation by imaging the expanding cloud after short free-fall durations. If the atom cloud does not start as a point source, a bias is introduced in the scale factor that differs from the simple point-source limit. We explored the scale factor deviation experimentally with different initial cloud sizes and present our understanding of this important systematic.**

Keywords—Atomic gravimeter; atomic gyroscope; compact inertial sensor; Point Source Interferometry; scale factor bias.

I. Introduction

Atom interferometers driven by laser pulses [1, 2] have demonstrated their ability to realize absolute measurements of rotation and acceleration with state-of-the-art sensitivity [3], accuracy [4] and bias drift [5] compared to other technologies. So far these results have largely been implemented in laboratory-size experiments, but current efforts are underway to develop more compact instruments for in-field inertial navigation and geodesy [6-8]. Usually, counter-propagating atomic sources are required to decouple phase shifts induced by rotation and acceleration [3], and atom motion along at least two axes is required to determine all six acceleration and rotation components. These requirements imply complex, multi-axis geometries with multiple atom sources. To accomplish the decoupling of acceleration and rotation and provide a path to a complete six-axis inertial sensor with a single atomic source, we extend the Point Source Interferometry (PSI) technique, so far demonstrated in a 10-meter tower [9], to the compact regime.

II. Point Source Interferometry

In our experiment, we use the usual Mach-Zehnder atom interferometer scheme where we first apply a Raman π/2-pulse to induce a spatial separation of the atomic wavepackets *via* a momentum transfer on one arm of the interferometer. Next, a Raman π-pulse is applied, simultaneously reversing both the internal and external states of the wavepackets. Finally, the wavepackets recombine *via* a second Raman π/2-pulse, and interfere when their final positions overlap. The laser phase of each pulse is imprinted on the atom phase, leading to a phase difference at the interferometer output [2, 3]

$$\Delta\Phi = \Delta\Phi_{\mathrm{acc}} + \Delta\Phi_{\mathrm{rot}} = \vec{k}_{\mathrm{eff}} \cdot \vec{a}T^2 + 2\vec{\Omega} \cdot \left(\vec{k}_{\mathrm{eff}} \times \vec{v}\right)T^2, \quad (1)$$

which is reflected in the final atomic level populations. Here $\hbar\vec{k}_{\mathrm{eff}}$ is the effective momentum transferred to the atom ($\sim 2\hbar\vec{k}_{\mathrm{opt}}$, where $\vec{k}_{\mathrm{opt}}$ is the wavevector of the light), $\vec{v}$ is the atom velocity, T is the interrogation time between two consecutive Raman pulses, and $\vec{a}$ and $\vec{\Omega}$ are the apparatus acceleration and rotation. In PSI, we use the point-source approximation to describe the transverse atomic velocity $\vec{v}_{\mathrm{trans}} = \vec{r}/2T$, with $\vec{r}$ the final transverse atom position, and re-write the now spatially-dependent phase as:

$$\Delta\Phi(\vec{r}) = \vec{k}_{\mathrm{eff}} \cdot \vec{a}T^2 + \vec{\Omega} \cdot \left(\vec{k}_{\mathrm{eff}} \times \vec{r}\right)T. \quad (2)$$

Since the cloud contains a range of initial velocities, a rotation of the apparatus will induce a phase gradient in the cloud; while an acceleration will change the overall phase. It

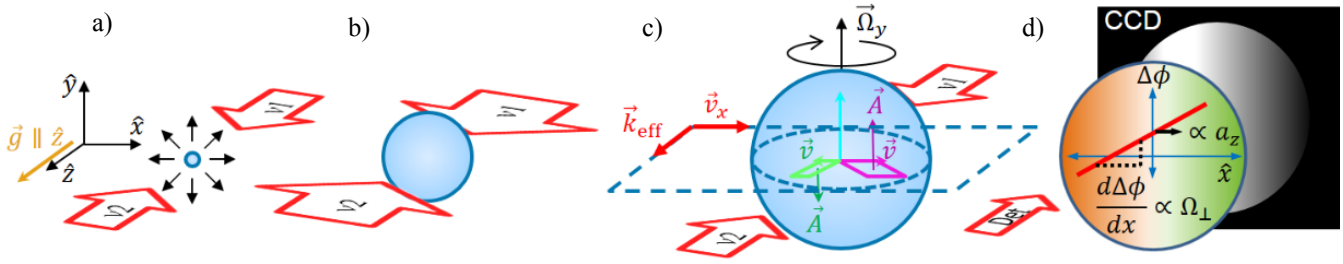

Fig. 1. The first three panels illustrate the Point Source Interferometry scheme with the expanding atomic cloud during a Mach-Zehnder sequence of Raman light pulses. The last panel represents the absorption detection and the extraction of the phase offset for acceleration and phase gradient for rotation.

978-1-5090-0720-2/16/$31.00 ©2016 IEEE

follows that a spatially resolved measurement of the interferometer phase can determine both rotation and acceleration. The signal appears in the spatial distributions of the final populations of the hyperfine states $|F = 1\rangle$ and $|F = 2\rangle$ due to the perfect match introduced between the internal and external states during a stimulated Raman transition [1].

III. Experimental Set-up

We realize a 3D magneto-optical trap (MOT) from a ^{87}Rb vapor inside a glass vacuum cell. With MOT beams having a radius at $1/e^2$ of 3.5 mm, we obtain 9×10^6 atoms at 5 µK with approximate Gaussian widths of $\sigma_x = 350$ µm and $\sigma_y = 220$ µm [10]. We then release the atoms from the trap and pump all the atoms in the $|F = 1, m_F = 0\rangle$ state to avoid sensitivity to stray magnetic fields to first order.

During the free fall, we apply the Mach-Zehnder sequence of light pulses. To split and recombine the interferometer arms, we use stimulated Raman transitions, in which two photon momenta are transferred to an atom while simultaneously changing its internal hyperfine state. The geometry of each Raman frequency component is described in Fig. 1 by the two red arrows in a counter-propagating configuration. To simulate the apparatus rotation, we tilt the retro-reflecting mirror of one of the Raman beams during the interferometer sequence [11].

We sketch the interferometric sequence in Fig. 1 with the first Raman π/2-pulse (a), the Raman π-pulse (b), and the second Raman π/2-pulse (c). Then the last panel (d) represents the absorption detection. The gravity $\vec{g}$ is along $\vec{z}$ but for simplicity the cloud's fall is not shown. The thermal expansion of the cloud leads to multiple interferometer trajectories in all the directions. Due to the scalar product in the rotation phase shift, the relevant trajectories are in the plane perpendicular to the rotation axis, *i.e.* (*x,z*) or (*y,z*) for a rotation axis $\vec{\Omega}_y$ or $\vec{\Omega}_x$ respectively. Those planes are determined by the effective momentum transferred to the atoms and the atom velocity perpendicular to both the rotation axis and the Raman axis. For each interfering atom, the area $\vec{A} = \hbar/m\,(\vec{k}_{\text{eff}} \times \vec{v})T^2$ enclosed by the two interferometer arms and therefore the rotation phase shift depend on the atom's initial velocity, as shown in Fig. 1 c). Then, in the point-source limit, the correlation between the atom's initial velocity and final position induces a phase gradient across the atomic cloud. We detect this phase gradient by imaging the populations in $|F = 2\rangle$ and in $|F = 1\rangle + |F = 2\rangle$ on a CCD. The CCD is located at the bottom of the glass cell, imaging the plane (*x,y*), while the Raman beams are vertically aligned along $\vec{z}$.

Thus, with only one cold atom source, we measure two rotation axes perpendicular to the Raman beams' axis ($\vec{x}$ and $\vec{y}$) through the phase gradient and one acceleration axis along the Raman axis ($\vec{z}$) through the phase offset. For an inertial sensor, if the apparatus rotations are not perpendicular to or if the apparatus acceleration is not collinear with the Raman beams' axis, the instrument will measure only the projection of the rotation or acceleration onto the principal axis defined by the Raman beams while we expect no blurring or any change in the fringe contrast.

An important feature in our compact device is the short free-fall duration during which we apply the interferometer sequence.

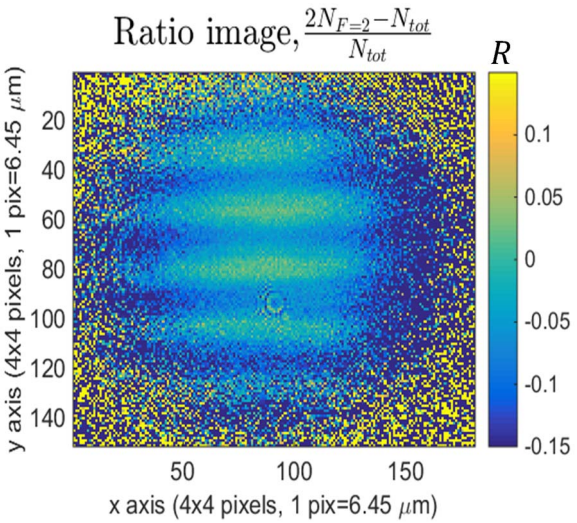

Fig. 2. Spatially resolved interference fringes induced by a rotation Ω = 136 mrad/s around *x* for a total interrogation time 2T = 16 ms. The ratio image presented here is an average of 30 images and the contrast is 10%.

This constrains the maximum expansion factor, which is defined by the ratio of the initial cloud size to the final cloud size $\sigma_{\text{final}}/\sigma_{\text{initial}}$. In our experiment, the expansion factor is limited to about five at maximum. This expansion factor expresses the importance of the initial cloud size compared to the cloud temperature and the free-fall duration. When the expansion factor is small, the correlation between each atom's initial velocity and final position that leads to the spatial fringe pattern is blurred by the initial atomic cloud extension. We intuitively expect this blurring to cause a loss of contrast. Nonetheless, we also find an interferometer phase gradient $\vec{k}$ that depends on the initial cloud's size, as described in the following.

IV. Spatially Resolved Fringes

Now, we describe the phase gradient extraction from state population images and the scale factor measurement to show that the phase gradient depends on the initial cloud's size.

A. Normalized images

The spatial distribution of atoms in each hyperfine state, $N_{F=1}$ and $N_{F=2}$, is determined from two absorption images: a first shadow image of the $|F = 2\rangle$ population and a second shadow image of the full population in both $|F = 1\rangle$ and $|F = 2\rangle$ states acquired after repumping the atoms in $|F = 1\rangle$ into the $|F = 2\rangle$ state. We plot in Fig. 2 the ratio image, defined by $R = (N_{F=2} - N_{F=1})/(N_{F=1} + N_{F=2})$, which allows us to suppress the cloud shape, while keeping the rotation induced fringes visible. The contrast in Fig. 2 is twice the contrast in transition probability.

Although the fringes are clearly visible, a residual cloud shape is still present on the ratio images. It comes mainly from an unavoidable short delay between the images of the populations in $|F = 2\rangle$ and $|F = 1\rangle + |F = 2\rangle$, leading to different cloud sizes between these two images. The residual cloud shape prevents us from performing a simple sinusoidal fit to the fringe that would be independent of the cloud shape. This

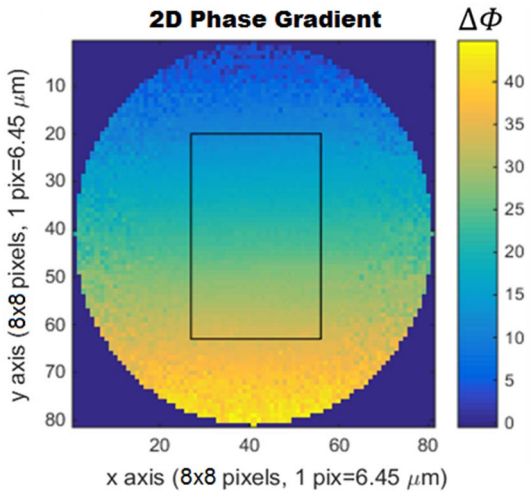

Fig. 3. Extracted phase gradient k = 10.08 ± 0.1 rad/mm along y induced by a rotation of Ω = 171 mrad/s around x for 2T = 16 ms.

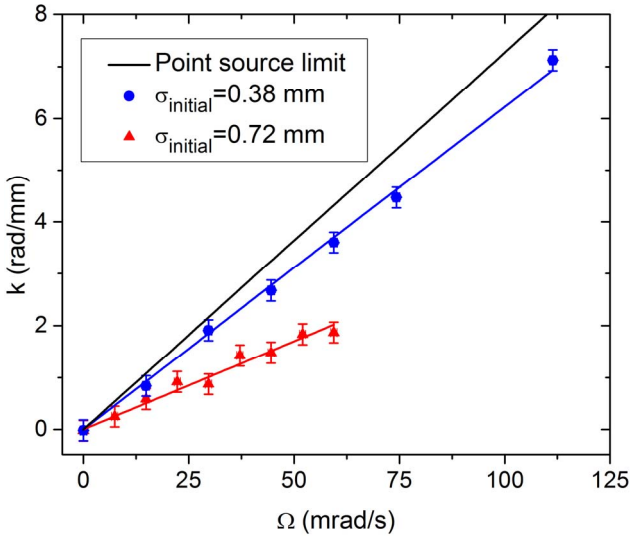

Fig. 4. Scale factor measurement k *vs* Ω for two different initial cloud sizes, and the theoretical point-source limit, for 2T = 16 ms. k is measured along x, while Ω is rotated around y. Dotted lines are linear fits to data.

independence is important to avoid introducing a systematic error on the fringe period, which would result in a bias in the phase gradient extraction.

B. Phase gradient extraction

To extract the phase gradient in a model independent way, we take several ratio images with a different phase offset. We record a collection of images while the overall phase is scanned over several interferometer fringes. This is experimentally done by scanning the frequency ramp α applied between the two frequencies of the Raman transitions to compensate for gravity. The collection of ratio images allows us to plot for each pixel the measured transition probability as a function of the applied phase offset ($\vec{k}_{\text{eff}} \cdot \vec{a} - 2\pi\alpha$) and fit a sinusoid to it. From the fit parameters, we reconstruct a map of the interferometer phase as a function of position, as shown in Fig. 3. Finally, we fit a 2D plane to the central region indicated by the black rectangle in Fig. 3 to extract the measured phase gradients along x and y, which is dependent on the applied rotation's direction and amplitude.

C. Scale factor measurement

For the spatially-resolved measurement of the rotation, the scale factor is the proportionality constant linking the applied rotation and the measured fringe period, or phase gradient, and expressed as $F = k/\Omega$. In order to determine the scale factor, defined by the slope of k *vs* Ω, we measure the phase gradients k_x for different rotations Ω_y. By measuring the phase gradients for two different initial cloud sizes, σ_x = 350 μm and σ_x = 720 μm, we observe a strong effect of the finite cloud size on the scale factor for cases where the cloud size has only increased by an expansion factor of $\sigma_{\text{final}}/\sigma_{\text{initial}} \approx 3$ or 1.5. As can be seen in Fig. 4, the scale factor changes by a factor of two between these two initial cloud sizes.

We have developed a model that takes into account the finite cloud size and predicts the scale factors with an extended atomic source [12]. If the initial cloud is modeled with a spatial Gaussian distribution and a thermal distribution having a uniform temperature, the scale factor is described by

$$F = \frac{2T^2}{T_{\text{tot}}} k_{\text{eff}} \left(1 - \frac{{\sigma_{\text{initial}}}^2}{{\sigma_{\text{final}}}^2}\right), \quad (3)$$

where T_{tot} is the total free fall duration, and the final cloud's size depends on the initial cloud's size and temperature.

From this model, we see that in this short free-fall regime the extended source causes a large deviation on the scale factor from the point-source limit. Accurate determination of the scale factor and hence the rotation rate would therefore require the source phase-space density to be considered. More importantly, these observations imply that size and temperature fluctuations of the initial atom cloud also add to the gyroscope scale factor instability. In an inertial navigation system, the scale factor stability is a critical factor of the gyroscope performance.

V. Conclusion

In this paper, we have shown that spatially resolved fringes can be obtained in a compact regime, even if the expansion factor is lower than two. We measured rotations along two axes and acceleration along one axis with only one cold atom source. To measure all six inertial components, three pairs of Raman beams would be needed, one along each axis, leading to six measured phase gradients and three measured shifts, obtained sequentially. There is hence a redundancy in the rotation measurements, useful to compare absolute rotations or implement corrections on an axis-by-axis basis. We also showed that the scale factor is modified by the extension of the initial cloud for a low expansion factor, introducing a deviation from the point-source model initially developed to describe this interferometric scheme.

As a mid-term objective, we intend to address the performance limits of this interferometer with respect to sensitivity, dynamical range and scale-factor stability. We expect the upper limit of the rotation dynamic range to be determined by the atomic cloud's initial size and the lower limit to be set by atomic shot noise. With a better signal-to-noise ratio, we should be able to measure the Earth's rotation to characterize the gyroscope instability. This would allow us to also characterize the scale factor instability introduced by the finite-size effect with a cold-atom source provided by a MOT.

We hope ultimately to develop a compact inertial sensor that would complement other sensing technologies with the potential stability provided by atoms.

ACKNOWLEDGMENT

This work is funded by NIST, which is a U.S. government agency. The manuscript is not subject to copyright.

REFERENCES

[1] C. J. Bordé, "Atomic interferometry with internal state labelling," Physics Letters A, vol. 140, no. 1, pp. 10 – 12 (1989).

[2] M. A. Kasevich and S. Chu, "Atomic interferometry using stimulated Raman transitions," Phys. Rev. Lett., vol. 67, no. 2, pp. 181 – 184 (1991).

[3] T. L. Gustavson, P. Bouyer, and M. A. Kasevich, "Precision rotation measurements with an atom interferometer gyroscope," Phys. Rev. Lett., vol. 78, no. 11, pp. 2046 – 2049 (1997).

[4] A. Peters, K. Chung, and S. Chu, "High-precision gravity measurements using atom interferometry," Metrologia, no. 1, vol. 38, pp. 25 – 61 (2001).

[5] D. S. Durfee, Y. K. Shaham, and M. A. Kasevich, "Long-Term Stability of an Area-Reversible Atom-Interferometer Sagnac Gyroscope," Phys. Rev. Lett., vol. 97, no. 24, pp. 240801 (2006).

[6] R. Geiger, V. Ménoret, G. Stern, N. Zahzam, P. Cheinet, B. Battelier, A. Villing, F. Moron, M. Lours, Y. Bidel, A. Bresson, A. Landragin, and Ph. Bouyer, "Detecting inertial effects with airborne matter-wave interferometry," Nature Commun., no. 2, pp. 474 (2011).

[7] M. Hauth, C. Freier, V. Schkolnik, A. Senger, M. Schmidt, and A. Peters, "First gravity measurements using the mobile atom interferometer GAIN," Applied Physics B, vol. 113, no. 1, pp. 49 – 55 (2013).

[8] T. Farah, C. Guerlin, A. Landragin, Ph. Bouyer, S. Gaffet, F. Pereira Dos Santos, S. Merlet, "Underground operation at best sensitivity of the mobile LNE-SYRTE cold atom gravimeter," Gyroscopy and Navigation, vol. 5, no. 4, pp. 266 – 274 (2014).

[9] S. M. Dickerson, J. M. Hogan, A. Sugarbaker, D. M. S. Johnson, and M. A. Kasevich, "Multiaxis Inertial Sensing with Long-Time Point Source Atom Interferometry," Phys. Rev. Lett., vol. 111, no. 8, pp. 083001 (2013).

[10] G. W. Hoth, E. A. Donley, and J. Kitching, "Atom number in magneto-optic traps with millimeter scale laser beams," Optics Letters, vol. 38, no. 5, pp. 661 – 663 (2013).

[11] S.-Y. Lan, P.-C. Kuan, B. Estey, P. Haslinger, and H. Müller, "Influence of the coriolis force in atom interferometry," Phys. Rev. Lett., vol. 108 pp. 090402 (2012).

[12] G. Hoth, B. Pelle, S. Riedl, J. Kitching, and E. A. Donley, in preparation.